A high-resolution map of Hawaiian ULVZ morphology from ScS phases

Jennifer Jenkins[a,1,*], Sima Mousavi[b], Zhi Li[a], Sanne Cottaar[a]

[a] *Bullard laboratories, University of Cambridge*
[b] *Australian National University*

Abstract

We use core reflected ScS waves sensitive to a broad region of the core-mantle boundary beneath Hawaii to create the first high-resolution map of the Hawaiian ultra-low velocity zone (ULVZ). Positive ScS-S differential times are used to identify regions of strong slow velocity anomalies in the lowermost mantle, and the presence of pre/post-cursors around the main ScS phase confirm the sharp top of a basal ULVZ layer. Pre/post-cursor arrivals are mapped into a volume across their region of sensitivity to produce a detailed image of ULVZ morphology. The variability observed across the ULVZ can be interpreted in terms of varying height or velocity reduction, but the large range of velocity variations required to explain observations suggests that most variability reflects varying layer thickness.

The Hawaiian ULVZ is observed to be a large-scale regional feature of varying height (~5-25km) extending across a wide area along the edge of the Pacific large low-velocity province (LLVP). Variability in previous models of the Hawaiian ULVZ can be explained by studies imaging different parts of this strongly variable, large-scale feature. Maximum ULVZ thicknesses (no taller than 30km) are found in a flat-topped, steep-sided region on the order of 1000km in di-

*corresponding author
Email address: `jj405@cam.ac.uk` (Jennifer Jenkins)

ameter located west of Hawaii. This feature is coincident with the previously identified Hawaiian mega-ULVZ, and is interpreted to represent the root of the Hawaiian plume, which is offset from the volcanic surface expression. A tall, asymmetric ridge of ULVZ material is observed to the east of Hawaii. Both regions of maximum ULVZ heights are bounded by the Pacific LLVP to the south, and fast seismic velocity anomalies interpreted as slab remnants to the north. This points to a potential geodynamical scenario where dense ULVZ material is pushed by subducted slab remnants into thicker piles against LLVP margins.

Keywords: Ultra-low velocity Zone, Hawaii, plume, Core-mantle boundary

1. Introduction: Ultra-low Velocity Zones

Ultra low velocity zones (ULVZs) are enigmatic seismic features found on the core-mantle boundary (CMB). While seismic wave-speeds in the majority of the Earth's mantle vary by only plus or minus a few percent from 1D radial predictions, ULVZs show wave-speed reductions of $5-50\%$ in shear-wave velocity and $5-25\%$ in compressional-wave velocity (Yu and Garnero, 2018). ULVZs are usually observed in local waveform studies as small isolated patches of material, 100s of km wide and only tens of km high, and are below the resolution of long-wavelength seismic tomographic models.

It has been suggested that ULVZs may be preferential located at the edges of (and possibly within) the two large-scale low-velocity features of the CMB landscape – large low-velocity provinces (LLVPs). There have also been suggestions of a link between particularly large "mega"-ULVZs and the base of major mantle plumes, with observations beneath Iceland (Yuan and Romanowicz, 2017), Hawaii (Cottaar and Romanowicz, 2012), Samoa (Thorne et al., 2013) and Galapagos (Cottaar and Li, 2018). This had lead to the hypothesis that these structures could act as plume anchors, and may be the source of anomalous geochemical observations in some hotspot lavas (Mundl et al., 2017; Harrison et al., 2017).

The underlying cause of ULVZs is not known, but velocity reductions of such magnitude require extreme variations in either temperature or composition, or, more likely, some combination of both. A variety of hypotheses have been proposed including: the presence of partial melt, association with subducted material in the form of metallic slab-derived melts (Liu et al., 2016) or partially molten basaltic piles (Pradhan et al., 2015), reactive material from the Earth's core (Buffett et al., 2000; Otsuka and Karato, 2012) or iron-enriched remnants of a basal magma ocean from early in Earth history (Labrosse et al., 2007). Geodynamic modelling shows that ULVZs formed of either partial melt or a compositional distinct dense material, are predicted to interact with other lower-mantle structures in different ways, resulting in different global distributions and morphologies (e.g. Li et al., 2017). Thus good seismic constraints on the detailed shape of ULVZs and their relationship to LLVPs, remnant slabs and plumes on the CMB will help to identify their underlying cause and their role within the large-scale mantle convecting system.

1.1. Seismic imaging of the Hawaiian ULVZ

Many previous seismic observations of the Hawaiian ULVZ have been made using a variety of data types sensitive to different areas around Hawaii. Estimates of the ULVZs lateral extent, height (5 – 80km), velocity contrast (Vs -3 – -30%) and even location (to the west, south or East of the Hawaiian islands) vary widely between studies (see Supplementary Table 1 for a summary). This could be the result of the different types of observations and modeling approaches used. Alternatively variability could represent sampling of a large-scale structure with varying velocity contrast and/or topography, as hinted at by some of the more recent studies (Zhao et al., 2017).

To the West of Hawaii, studies have mapped a so-called "mega"-ULVZ using diffracted waves grazing the CMB (To et al., 2011; Cottaar and Romanowicz, 2012; Kim et al., 2020). The long distances over which diffracted waves sample the CMB means that they are unable to determine the exact location and shape of ULVZ structure. Proposed models are restricted to simple cylindrical or gaussian shapes, with trade-offs between the radius and velocity contrast of structure.

To the southeast of Hawaii, the CMB has been sampled by reflecting waves (ScS and PcP phases) recorded at stations in the US (Mori and Helmberger, 1995; Kohler et al., 1997; Revenaugh and Meyer, 1997; Lay et al., 2006; Avants et al., 2006; Hutko et al., 2009; Zhao et al., 2017; Sun et al., 2019). These phases have a much finer horizontal-resolution, only being sensitive to CMB structure around the wave's bounce-point, but this also makes them limited in terms of data coverage. Thus most studies using reflected waves have been restricted to small regional observations. Unlike diffracted waves, reflected phases provide good lateral constraints, but have trade-offs between the height and velocity contrast of modeled structure.

Here we concentrate on mapping the detailed shape of the Hawaiian ULVZ using the high lateral resolution provided by CMB reflected waves, making use of the large seismic station deployments of the USArray and Alaskan transportable-array. The recent movement of USArray into Alaska, provides new data coverage of the CMB west of Hawaii that has previously only been mapped using diffracted waves. This data set allows us to map out the broad lateral extent and complex 3D morphology of the Hawaiian ULVZ across a large region using a consistent dataset and analysis approach. We interpret our observations in the context of geodynamic models and long-wavelength velocity structure imaged in tomographic models to infer ULVZ properties and investigate how these features interact with other CMB structures.

2. Seismic Data and initial processing

2.1. Core reflected S waves

We use S-waves that bounce off the CMB (ScS phases, Figure 1-inset) to make observations of ULVZ structure beneath Hawaii using stations and events separated by epicentral distances of ∼65-87°. Beyond 80° S and ScS phases start to interfere and eventually merge as S-waves that diffract along the CMB. We extend the usable data range up to 87° by deconvolving an estimated S-source waveform (as detailed in 2.3). We use transverse component seismograms which record larger amplitude S_H waves and avoid complications of P-S_V converted phases set at ULVZ interfaces.

2.2. Events and stations: cross Pacific raypaths

We limit events to large M_W (>5.5), deep earthquakes (> 100 km) occurring in Fiji/Tonga/Papua New Guinea between 2006-2020. Waveforms are considered at all simultaneously running stations in Alaska, Canada and the US that are within 65-87° of the event. The majority of the 2172 seismic stations used are part of either the western half of the USArray deployment (2009-2012) or the Alaskan transportable array (2015-2020), with additional contributing instruments from many smaller deployments (Figure 1). In total 62 events produce clear S and ScS arrivals observable above noise and are selected for further analysis. These station–event pairs have ScS CMB bounce-points sensitive to a broad region beneath the Hawaiian islands and along the northern edge of the Pacific LLVP (Figure 1).

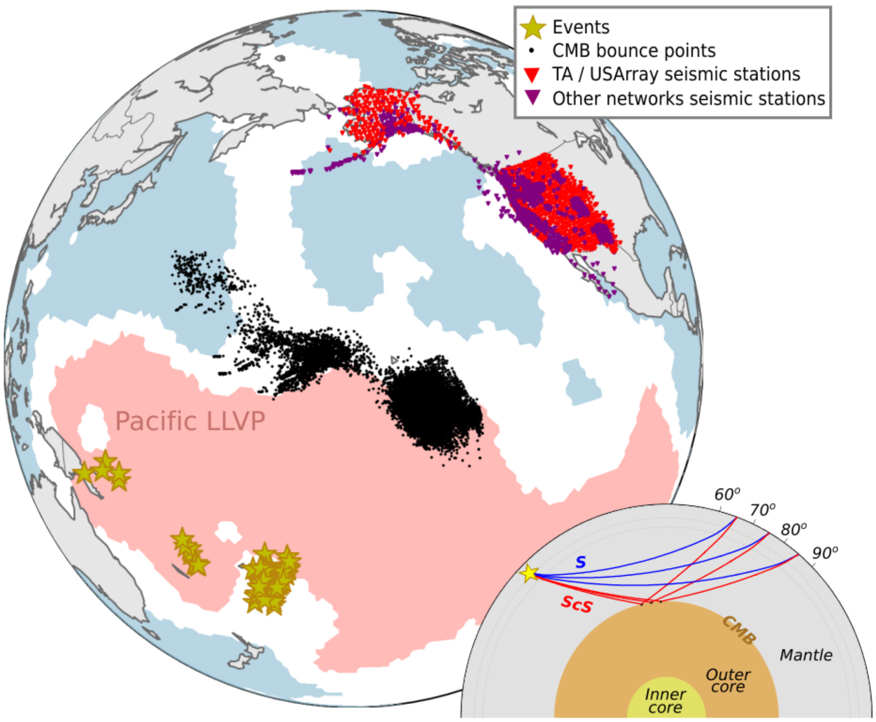

Figure 1: Map showing locations of events (yellow stars), stations (purple and red triangles) and CMB bounce-points of ScS rays (black dots), on top of the tomographic vote map of Lekic et al. (2012) at the CMB. Pink regions show where > 4 tomographic models agree on the presence of slow velocity anomalies, and blue regions where > 4 models agree on the presence of fast velocity anomalies. Inset - Raypaths of S and ScS phases within the distance range considered in this study.

2.3. Initial Data Processing and S-source wavelet removal

During initial data processing horizontal components are rotated from North/East to Radial/Transverse, instrument response is removed, traces are cut from 30s before to 80 s after the S-wave arrival and data is filtered between 2.5-30 s (0.03-0.4Hz) or 5-30 s (0.03-0.2Hz) depending on the analysis method used. These bands allow us to capture the range of frequencies present in ScS arrivals which show strong frequency content between 2.5-10 s in spectrograms. Data are manually checked and discarded if clear S and ScS arrivals are not observable above noise.

We deconvolve the S-source waveform from the data, which, due to near perfect reflection at the CMB, is predicted to be almost identical in shape to ScS waveforms and associated multiples. S-sources are estimated for each event by stacking S-waves recorded on stations $< 80°$ from the event - where there is no S/ScS phase interference. Stacked S-source waveforms are then deconvolved from data via iterative time-domain deconvolution (Ligorria and Ammon, 1999). This collapses all relevant phase arrivals (both S and ScS) to narrow Gaussian peaks of a user defined Gaussian width (G) (Figure 2). G is defined as twice the maximum frequency within the filtered range: G=0.8 for 2.5-30 s band and G=0.4 for 5-30 s. An example of data before/after source deconvolution is shown in Figure 2. Data are manually checked for clear S-wave sources and stability of deconvolution results. A total of 8149 waveforms are selected for analysis.

Removing the S-wave source not only extends the use-able distance range of observations from $\approx 80°$ up to approximately $\approx 87°$, but also allows observation of small amplitude, closely spaced pre/post-cursors around the ScS phase. After deconvolution, phase arrival picking is simplified to identifying the maxima of Gaussian peaks and we are able to directly compare and stack data from different events, since variable source waveforms are reduced to a common shape.

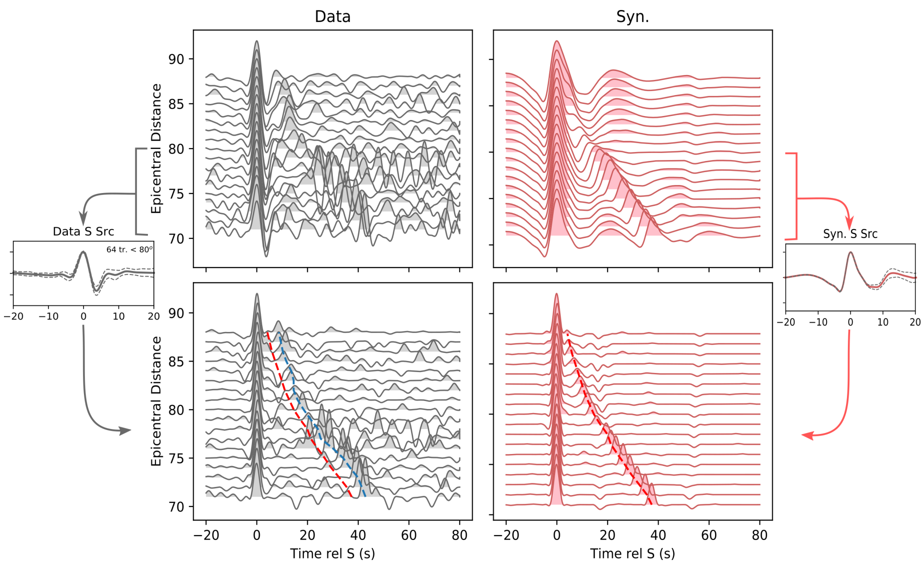

Figure 2: Top panels – waveforms at a range of epicentral distances centred on the S-wave arrival filtered 5-30s for synthetic data (pink) generated for a 1D PREM model using AxiSEM syngine (Nissen-Meyer et al., 2014; IRIS-DMC, 2015) and real data (grey) from an event occurring on 2018-09-30 near Fiji – recorded at stations in the Alaskan transportable array. Bottom panels – Waveforms after deconvolution of S-source waveforms (shown at either side). Red dashed lines show predicted arrival times of ScS phases in a 1D PREM model and blue dashed lines show delayed ScS arrivals in real data.

3. Methods: Analysis of core-bouncing waves

We consider two methods to analyse CMB structure using source deconvolved ScS arrivals: ScS-S differential time measurements (referred to as (ScS-S)^{diff}) and observations of ScS pre/post-cursors.

3.1. ScS-S Differential Times

At the epicentral distance range considered, S and ScS waves sample very similar paths within the upper mantle on both source and receiver side (Figure 1-inset). The only significant divergent of raypaths comes in the lower-mantle, thus measurements of ScS-S arrival times are sensitive to lowermost mantle structure between the turning point of the S-wave and the CMB (Figure 3a). Observed ScS-S arrival times are compared to ScS-S times predicted from a known velocity model, such that we measure the differential time:

$$(ScS-S)^{diff} = (ScS\text{–}S)_{obs} \text{–} (ScS\text{–}S)_{pred} \tag{1}$$

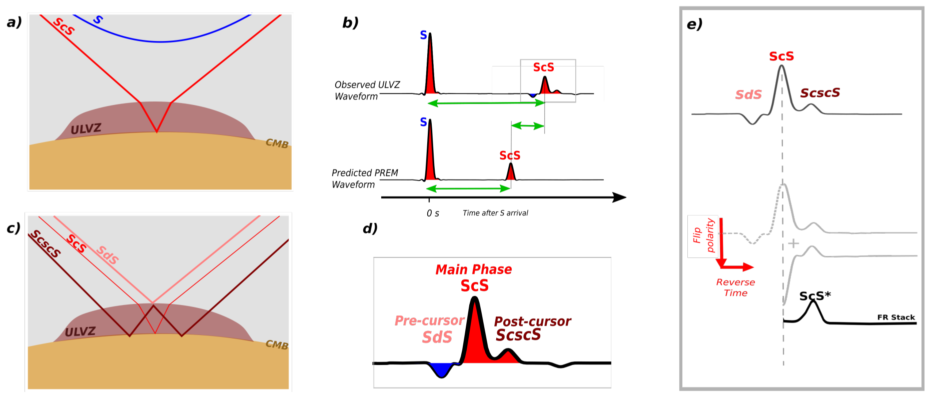

Figure 3: a) Raypaths of direct S waves and core reflected ScS phases interacting with a ULVZ. b) example of source deconvolved S and ScS arrival differences observed with and without the presence of an ULVZ. c) Cartoon diagram of the raypaths of pre/post-cursors around the main ScS phase generated by a sharp-topped ULVZ d) zoom in around ScS arrival showing pre/post-cursors arrivals. e) Explanation of Flip-Reverse stacking procedure used to enhance pre/post-cursor arrivals.

Where there is no anomalous lower-mantle structure differential times should be near zero. In the presence of an ULVZ positive differential times of several seconds are expected, due to the delay of the ScS$_{obs}$ (Figure 3b).

We measure ScS and S arrival times in S-source deconvolved data within the 5-30 s frequency band. Phases are automatically picked at the maximum amplitude in a time window around the predicted arrival times estimated from the Preliminary Earth Reference Model (PREM) (Dziewonski and Anderson, 1981). Automatic picks are manually checked and adjusted for mis-picking comparing raw and deconvolved data.

ScS-S times are predominantly sensitive to structure between the S-wave turning point, this is generally the bottom few 100s of km, but can be up to ≈1000km at the lower end of the epicentral distance range. Accordingly differential times represent an integrated time difference caused by all mantle material within this depth range. Since we are interested in extreme structures on the CMB, we correct differential times for predictions of broad-scale 3D mantle structure based on tomographic models. (ScS-S)$_{pred}$ times are computed in 1D reference model PREM and 3D corrections are calculated for a range of recent global shear-wave tomographic models:

1. SEMUCB-WM1 (French and Romanowicz, 2014)
2. GyPSuM (Simmons et al., 2010)
3. HMSL-S06 (Houser et al., 2008)
4. SPani_vs (Tesoniero et al., 2015)
5. TX2011 (Grand, 2002)

Velocity structure within each model is extracted along S and ScS raypaths traced through PREM using ray-tracing software TauP (Crotwell et al., 1999). Extracted velocity anomalies along the raypaths give corrections to the (ScS-S)$_{pred}$ times for each model which are compared to (ScS-S)obs times.

3.2. ScS pre/post-cursors

In the presence of a sharp topped ULVZ, a negative polarity reflected phase off the ULVZ top precedes the ScS phase, while positive polarity post-cursors decreasing in amplitude follow the ScS phase from energy bouncing internally within the ULVZ (Figure 3c,d). The relative arrival time between pre/post-cursors and the main ScS arrival can be used to estimate ULVZ height and velocity reduction. However there is a direct trade-off between these parameters: a thick ULVZ with a weak velocity reduction produces the same arrival times of pre/post-cursors as a thin ULVZ with a strong velocity reduction.

Raypaths of pre/post-cursors and the ScS phase are highly similar throughout the entirety of their length except around the ULVZ itself. Thus unlike (ScS-S)^{diff} times, arrival times of pre/post-cursors (relative to the main ScS phase) depend only on velocities within the ULVZ.

3.2.1. Flip-Reverse Stacking

Pre/post-cursors are very small amplitude and are rarely observable above noise in a single waveform, thus stacking is required to enhance coherent signals and cancel out incoherent noise. Since we deconvolve the S-source waveform, we are able to stack data from many different sources.

Pre and post-cursors are predicted to arrive symmetrically in time but mirrored in polarity around the ScS phase (Figure 3d) and show negligible move-out with epicentral distance for a simple ULVZ layer. We enhance these small amplitude signals using the Flip-Reverse (FR) stacking technique developed by Zhao et al. (2017). This involves folding the seismic trace around the central ScS arrival, reversing the preceding section in time and polarity and stacking it with the subsequent section (Figure 3e). At high epicentral distances, where S and ScS arrivals are closely spaced in time, we mute traces around the main S arrival so it doesn't contaminate FR stacks. FR stacking not only emphasises small amplitude pre/post-cursory arrivals, it also cancels out the central ScS peak, reducing interference when these phases are closely spaced. FR stacking is applied to source deconvolved data in the 2.5-30s frequency band. The inclusion of higher frequencies produces noisier waveforms, but also allows us to observe closely spaced arrivals, increasing the vertical resolution of image-able structure. Vertical resolution depends on the velocity of the imaged ULVZ, but for a realistic range of velocities (-5 to -50% Vs), it varies between 10-2.5 km for the 2.5-30s band.

To combat high noise levels we only stack waveforms which meet the the following quality criteria:

- ScS amplitude is the largest peak in the trace
- ScS amplitude is > twice the average amplitude of the rest of the trace.

3.2.2. Geographic mapping of data: Common bounce-point stacks

We image the lateral variability of ULVZ structure by producing a weighted stack based on the bounce-points of ScS phases across our area of data coverage - a common bounce-point (CBP) stack. We create three CBP stacks using: 1) time-flipped pre-ScS traces, 2) post-ScS traces and 3) FR stacked-traces. A gridded stack region is defined covering the Hawaiian region from 150° to 230° longitude and -5° to 40° latitude sampled every degree. Each trace is added to every grid-point in the CBP stack which lies within the first Fresnel zone of a 2.5 s period ScS phase at its CMB bounce-point, with data weighted as a function of distance from the Fresnel zone centre (see Supplementary Material S2 and Figure S3 for details).

We automatically pick peaks considering observations across all three CBP stacks, if they: 1) are above two standard error of the mean in the FR CBP stack and 2) show consistent negative and positive amplitudes in pre-ScS and post-ScS CBP stacks respectively. With the assumption that a ULVZ will sit directly atop the CMB, cross-sections through the final stack are used to identify the first peaks in stacks above zero time that represent continuous features observable across large areas. Peaks defining such features are manually selected from auto-picks.

3.2.3. Height-Velocity HV stacking

We model potential ULVZ structure causing pre/post-cursor arrivals with a stacking technique we call Height-Velocity (HV) stacking. This is adapted from the commonly applied HK stacking method that models crustal thickness

(H) and Vp/Vs ratios (K) using Ps converted phases in crustal receiver function (RF) data (Zhu and Kanamori, 2000). To determine the more likely HV properties of the ULVZ, we take the following steps, as depicted in Figure 4:

1. For a grid of potential heights (H) and velocities (V), we sample the amplitudes at predicted arrival times within individual FR-stacked traces. Predicted times comes from lookup-tables based on synthetic data (Supplementary Material S1). Each grid illustrates the trade-off between H and V given by a single FR-stack.
2. (ScS-S)^{diff} measurements (averaged relative to 5 tomographic models) are used to generate a data mask for each trace, where H/V parameter combinations that produce larger (ScS-S)^{diff} times than observed are down-weighted.
3. Individual HV stacks and (ScS-S)^{diff} masks are averaged across all data.
4. A model trade-off curve is identified in the average HV stack. Bootstrapping is used to assess the data based error of curves, by calculating 200 iterations of the averaged HV stack including a randomly selected 70% of data.
5. The average HV stack is multiplied by the average (ScS-S)^{diff} mask to generate a final weighted HV stack, which can be used to identify likely models.

Unlike the Ps phases analyzed in crustal RFs, the two pre/post-cursors phases around ScS arrivals do not have unique model parameter trade-offs. Thus non-masked HV stacks cannot identify a single best-fit model, but define a range of possible parameters within a trade-off curve (Figure 4d). Including additional constraints contained in the (ScS-S)^{diff} mask, acts to remove multiple arrivals that could be misinterpreted as thicker structure (e.g. Figure 4d-f). In perfect synthetic data the (ScS-S)^{diff} mask excludes ULVZs with strong velocity reductions, allowing identification of the input model at the maximum amplitude in the stack (Figure 4f). However in real data, where (ScS-S)^{diff} measurements likely contain some remaining influence of additional mantle structure, we find that masks only act to reduce the likelihood of models containing very strong velocity reductions, leaving a range of potential models (Figure 7).

HV-stack trade-off curves constrain minimum and maximum bounds on ULVZ height for a range of realistic ULVZ velocity contrasts. Ideally, amplitudes of the pre/post-cursors could be used as independent constraints on the impedance contrast at the ULVZ top, but there are too many uncertainties related to amplitude observations for this to be implemented on real data, as discussed in section 5.4. If any additional independent data is available to constrain one parameter or the other a best-fit model can be defined, e.g. a prediction of velocity contrast based on a mineral physics interpretation, or an independent seismic constraint, such as the frequency dependence of S$_{diff}$ data (Li et al., 2019).

4. Results

4.1. (ScS-S)^{diff} measurements

We present 8149 point estimates of (ScS-S)^{diff} times sensitive to lower-mantle velocity structure (Figure 5a). To reduce data scatter, points are averaged in overlapping 50km radius geographical bins spaced every 25km containing at least 6 observations (Figure 5b).

Measurements are corrected for 3D velocity variation, using 5 tomographic models. While each individual correcting model leads to slight differences in the travel-time maps (see Supplementary section S3), certain areas are consistently observed to have large positive (ScS-S)^{diff} delays independent of correcting model. These are highlighted in a vote map (Figure 5c), which shows regions

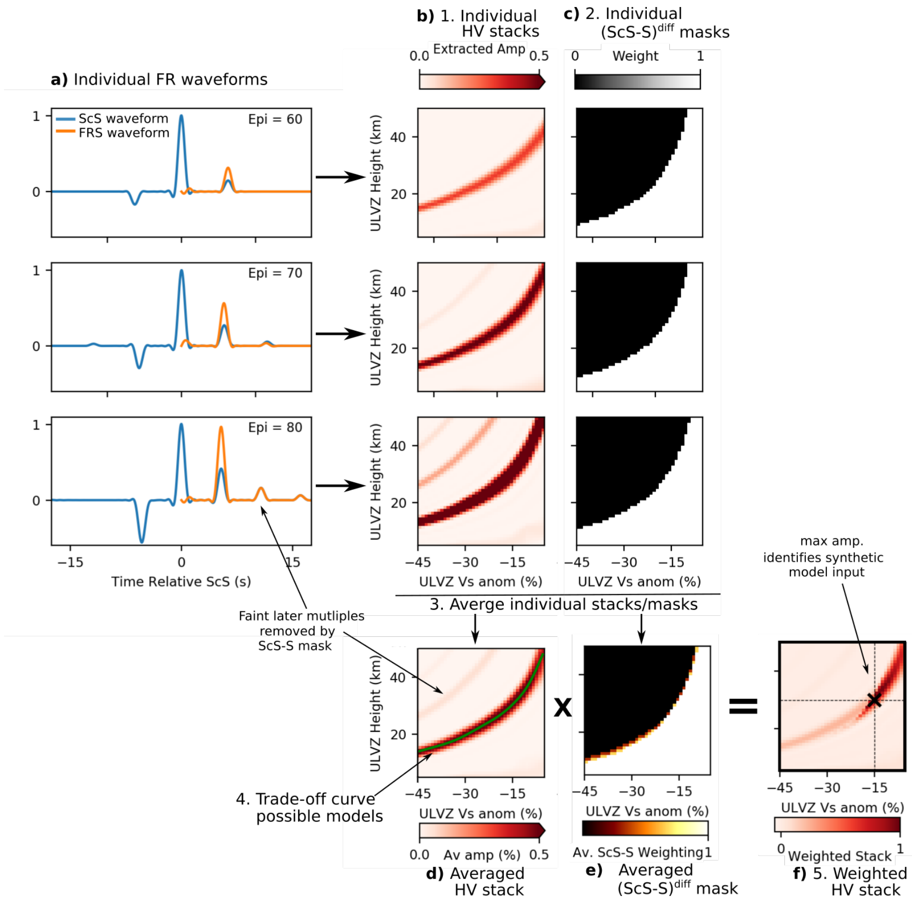

Figure 4: HV stacking methodology applied to synthetic seismic data generated for a ULVZ of height 30km with V_S reduction of -15%. a) FR stack waveforms, are sampled at the predicted times for a set of ULVZ models of varying height-H and velocity contrast-V to create b) HV stacks for each trace. Each piece of data also has c) a mask based on (ScS-S)^{diff} time generated which is used to down weight models inconsistent with this 2nd measurement. d) Individual HV stacks are summed and averaged to define the model trade-off curve. e) ScS-S masks are also averaged, and multiplied by the average HV stack to produce: f) the final weighted HV stack, showing a best-fitting model which identifies the input parameters.

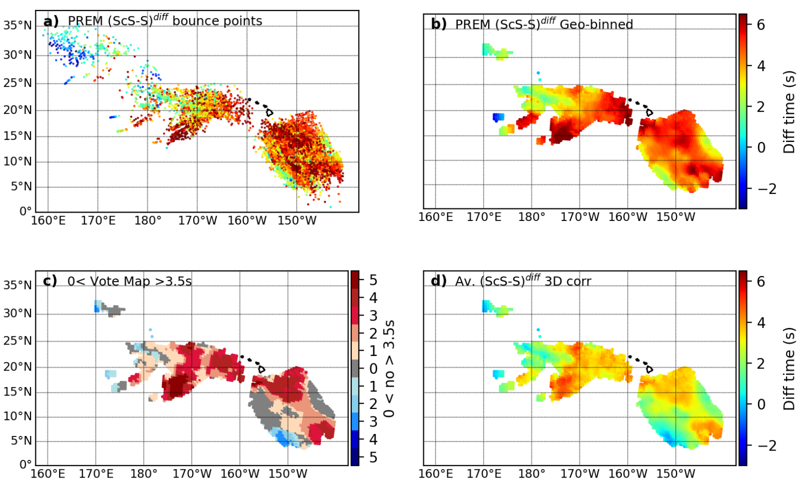

Figure 5: a) Bounce-points of 8149 ScS arrivals coloured as a function of (ScS-S)^{diff} time relative to 1D model PREM. b) Data averaged in geographical binning of 50km radius spaced every 25 km). c) Vote map showing number of models that agree on (ScS-S)^{diff} times >3.5 s after 3D corrections are applied (reds), and number of models agreeing on measurements <0 s (blues). d) (ScS-S)^{diff} 3D corrected times averaged over corrections based on 5 different tomographic models, geographically binned as in b.

where n models agree that (ScS-S)^{diff} times are >3.5 s in red. Application of 3D velocity model corrections reduce (ScS-S)^{diff} measurements compared to a 1D velocity model by 1-2.8 s on average (Figure S4), leaving significant delays of up to 7.5s which represent currently unaccounted for slow-velocity lower-mantle structure. Figure 5d shows (ScS-S)^{diff} corrected times averaged over all 5 models.

(ScS-S)^{diff} observations reveal large areas of the study area contain slow velocities in the lowermost mantle. Strongest delay times are observed west of the Hawaiian islands centred at approximately 15N, 170W (Figure 5). This region consistently shows the greatest delays across all correcting velocity models. Other areas of strong delays are observed surrounding the Hawaiian island chain and towards the southeastern limits of our data coverage.

At the NW and southern limits of data coverage we see slightly negative (ScS-S)^{diff} observations, indicating the presence of fast material in the lowermost mantle. However, these observations are more variable with choice of correcting tomographic model, thus we consider them less robust.

4.2. Common bounce-point stacks of ScS pre/post-cursors

Figure 6 shows cross-sections through the common bounce-point (CBP) stack of FR waveforms. The lateral extent, arrival times and amplitudes of picked continuous features are shown in Figures 6a and b. Picks represent first arrivals which are above two standard error in the FR CBP stack and show opposite polarities in pre-cursor and post-cursor CBP stacks. That is not to say regions outside of these picked features showed no potential structure. The cross-sections in Figure 6 show there is complexity in the stacks throughout, however we concentrate on identifying and mapping regions with the most robust pre/post-cursor arrivals that are likely to represent the top of a basal ULVZ layer directly above the CMB.

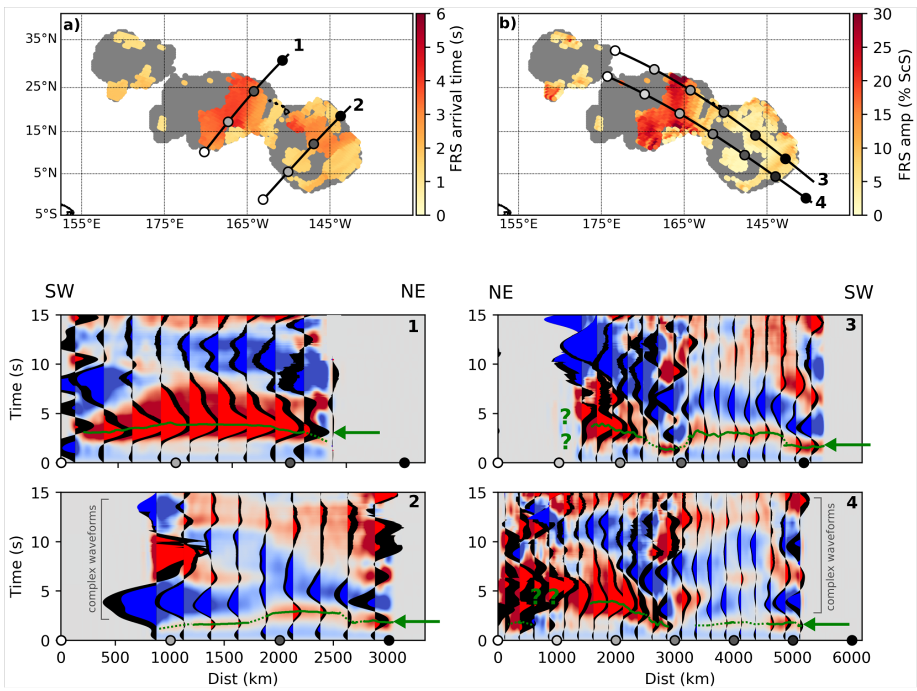

Figure 6: Maps of picked pre/post-cursor arrivals in CBP stacks of FR waveforms defining continuous basal layer coloured as a function of a) arrival time and b) arrival amplitude. Grey regions show where there is data coverage but there is no clear positive amplitude first arrival that meets these criteria. Orientations of the numbered cross sections are shown as black lines. 1-4) Cross-sections through the stack show continuous positive (red) and negative (blue) arrivals and extracted waveforms plotted every 250 km in black, with regions above 2 SE error coloured red for positive polarities and and blue for negative polarities. Green solid lines show picked arrivals above error and with correct polarities with are mapped out in a) and b). Dotted green lines show interpreted continuation of features where arrivals are present but not above error.

The broadest continuous feature, approximately 2000km by 1000km in size, is seen to the west of Hawaii, highlighted in Figure 6 section-1. Though we note that exact size of mapped features is influenced by our choice a 2.5s period to defines the Fresnel zone weighting function as explored in the supplementary text S4 and Figure S6. This feature shows the strongest arrival amplitudes of up to 30% of the main ScS wave, Figure 6b. From the southeast edge to the centre of the feature there is a gradual increase in arrival times (Figure 6 section-3). The northwestern edge is not easily defined due to highly complex waveforms (Figure 6 section-4), likely due to the reduced amount of contributing data in this area (Figure S2c). There are weak smaller delay time arrivals which are not above error in this region (Figure S5), suggesting the feature does not extend at the same level significantly further to the NW. A lack of data coverage further north and south means that this feature could potentially be more elongate towards the NE and SW.

The second clear region of continuous arrivals is located east of the Hawaiian islands (highlighted in Figure 6-sections 2 and 3), with the greatest delay times observed just adjacent to the island chain, Figure 6a. The amplitude of arrivals here (up to 10% of ScS) is significantly less than in the region west of Hawaii (Figure 6b). Across much of the region (particularly to the east of Hawaii) small delay time and amplitude arrivals are observable around $\approx$1.5 s which increase into the clear features already described, (dotted green lines in Figure 6 section-2 at 1000-2000km and section-4 between 3000-5000km). These observations suggest the presence of a distributed but thin/weak low velocity layer over much of the region, suggesting the Hawaiian ULVZ is a single large-scale but variable feature. Due to their small amplitude these arrivals are not always above error, and their small delay-times mean they often interfere with the main ScS arrival making it difficult to identify opposite polarities in pre and post-cursor CBP stacks. Thus we consider these observations less robust than those previously discussed and they are not represented in the map in Figure 6ab, but their full extent is mapped out in Supplementary Figure S5.

We note an area southeast of the Hawaiian islands showing complex waveforms in stacked data (Figure 6 sections 2 and 4). Here multiple strong amplitude positive and negative polarity arrivals potentially indicate the presence of layered slow and fast material.

4.3. HV stacks

We assess the potential height and velocity reduction of the Hawaiian ULVZ using HV stacks across five regions (Figure 7); component parts of weighted HV stacks are shown in Figure S7.

Regions B, C and D sample areas of strongly positive (ScS-S)^{diff} delay times, and lie within imaged structure in the CBP stacks. HV stacks for these areas show data can be modelled by an ULVZ layer with a height of 7-33 km (Figure 7bcd). Maximum amplitudes within the trade-off curve for stacks B and C are found at lower velocity reductions $<$20%, suggesting structure is within the upper height limits of the identified range $\approx$15-30km (Figure 7a - yellow bars). Assuming material within a ULVZ layer shows similar velocity across the region, and limiting the velocity reduction to 10-30% (as suggested by previous seismic studies of the area (Cottaar and Romanowicz, 2012; Zhao et al., 2017; Sun et al., 2019)), gives ULVZ thickness estimates of 11-23km (Figure 7a - red bars).

Stacks E and F sample regions of weaker, less robust arrivals in CBP stacks suggestive of a thinner/weaker continuous layer observed across much of the eastern part of the study region (Figure 7h). Region E shows positive (ScS-S)^{diff} measurements, while region F shows negative values (Figure 7g). Both areas have weak pre/post-cursor arrivals with small delay times in addition to later arrivals indicative of overlying structure. The earliest arrivals relating to a basal layer are just above the resolution limit for ULVZ structure (greyed out regions in Figure 7e-f). HV stacks indicate that these observations can be modeled with a thinner ULVZ layer (3-15 km), than observed in stacks B,C and D. Error estimates based on boot strap resampling of these data are higher, and amplitudes do not vary along the trade-off curve to help limit the possible velocity range. Limiting the possible range of velocity reductions based on previous predictions results in smaller estimated layer heights of 5-11km (Figure 7a-red bars).

We note that the amplitudes of pre/post-cursor arrivals are significantly smaller than those predicted for models that fall within the trade-off curves identified by arrival times in HV stacks (Figure S7) and discuss possible reasons for this in section 5.4.

5. Discussion

We find the strongest evidence for a broad ULVZ located west of the Hawaiian islands. This area shows the greatest (ScS-S)^{diff} delay times, and the strongest amplitude and most delayed pre/post-cursor arrivals. We refer to this as the western mega-ULVZ since it is coincident with the previously identified feature of Cottaar and Romanowicz (2012). The lateral extent of the mega-ULVZ is on the order of 2000km by 1000km, based on our limited data coverage but could be larger along the NE-SW long axis. HV stack trade-offs indicate structure is likely to be $\approx$20 km tall and is unlikely to be taller than 30 km for a realistic range of ULVZ velocity reductions.

East of the Hawaiian islands we find evidence of a ULVZ layer, of large lateral extent and variable height/velocity. Its highest point ($\approx$20km) is located just east of the Hawaiian islands, and is surrounded by a potentially continuous

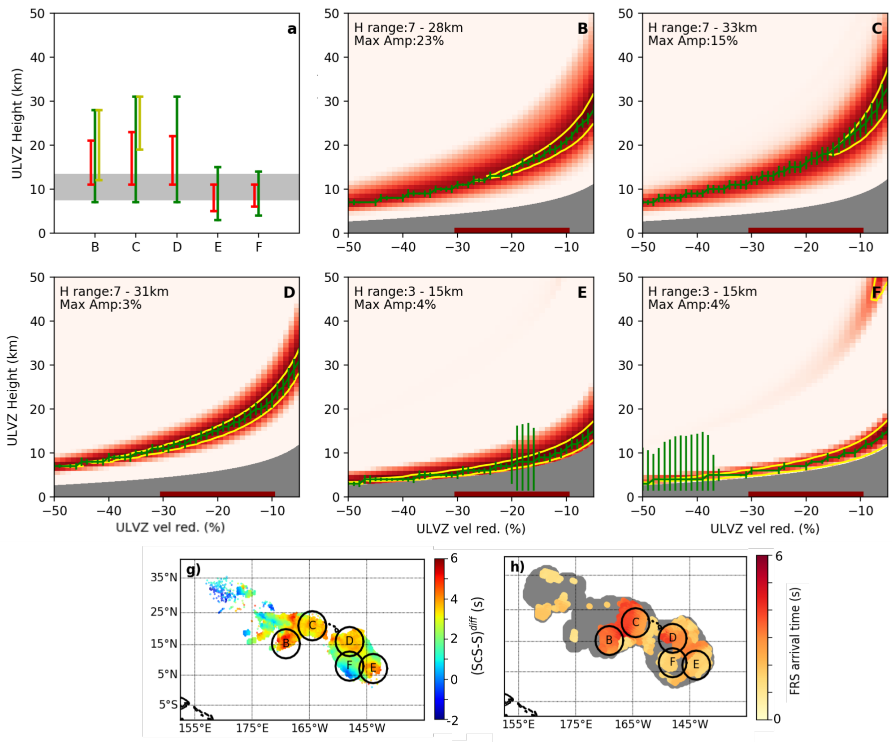

Figure 7: a) Predicted ULVZ layer height ranges for 5 stack areas. Green bars - full height range for velocity reductions between -5 to -50%, red bars - heights when velocity reductions are restricted to -30 to -10% based on estimates from previous seismic studies, yellow bars - height suggested by regions of strongest amplitude from (ScS-S)^{diff} weighting where present. Grey bar shows heights that fall within the trade-off curves of all five stack areas. B-F) show HV stacks used to define height and velocity contrast trade-off curves, with red colours showing strongest stacked amplitudes for given model parameters. Green lines show identified trade-off curves, green bars show 2 SD errors based on 200 boot-straps including a random 70% data, greyed out regions show models that are below the resolution limits of 2.5s period data. g) Locations of stacks are shown compared to averaged 3D corrected (ScS-S)^{diff} observations h) mapped structures in CBP stacks.

thinner 5-10km thick layer. We refer to this region as the Eastern ULVZ pile. In the southeast of our study area we observe complex waveforms indicating layered fast and slow material with the suggestion of a thin/weak ULVZ layer at the base.

5.1. Comparison to previous observations

Many previous studies have investigated the structure of the Hawaiian ULVZ using different seismic methods with different lateral sensitivities and trade-offs. These can broadly be split into three groups: those sampling the western mega-ULVZ, those sampling the complex southeastern region and those that cover a broader area east of the island chain. Studies explicitly discussed are plotted in Figure 9a, and all previous studies are summarised in Table S1.

5.1.1. Western mega-ULVZ

Studies that sample structure west of Hawaii have predominantly used S diffracted (S_{diff}) waves to identify a large region of extreme slow-velocities that sets up S_{diff} post-cursors (To et al., 2011; Cottaar and Romanowicz, 2012; Kim et al., 2020), and has been referred to as a mega-ULVZ. Since S_{diff} waves graze large areas of the CMB the precise location and shape of this structure is difficult to pinpoint. Cottaar and Romanowicz (2012) use beamforming techniques to better locate the ULVZs location, and waveform modeling to infer a simplified cylindrical shaped model ≈1000km in diameter. Their preferred location is within the structure we map out using pre/post-cursors and coincident with our observations of maximum $(ScS\text{-}S)^{diff}$ times. Their preferred ULVZ model parameters (20km high, velocity reductions of 15-25%) are also consistent with our observed trade-off limits which suggest a 20km high structure requires a 15% velocity reduction.

Most other studies that sample this region (Luo et al., 2001; To et al., 2011; Kim et al., 2020), suggest a taller structure with height estimates ranging from

50 to 100km, but still suggesting strong velocity reductions of between 10-25%. HV trade-off curves (Figure 7) indicate these tall but strong models are not compatible with our observations. It should be noted that we interpret only the basal layer in our CBP stacks, and the longer period S_{diff} waves used in previous studies could be influenced by reduced velocities above this basal layer.

5.1.2. Complex southeastern region

Many studies investigate the southeastern area of complex waveforms with a potential thin/weak ULVZ layer (Figure 6-sections 2 and 4) using reflected phases (PcP,ScS). This is due to the source-station paths from events in Fiji-Tonga recorded in the western US, which has been well instrumented for many years.

Early studies using PcP reflections suggested the presence of a 10-15km thick layer with Vp velocity reductions of -10% in this area (Mori and Helmberger, 1995; Kohler et al., 1997; Revenaugh and Meyer, 1997). Later studies moved towards using double-array stacking techniques to identify a variety of layered structures in the region (Avants et al., 2006; Lay et al., 2006; Hutko et al., 2009). All agree on the presence of a basal low-velocity layer which thickens towards the northeast, away from the LLVP centre. This is consistent with our observation in CBP stacks of a thinner 5-10km layer (Figure 7F) that gradually thickens to 10-20km (Figure 7D), as observed in Figure 6 section-2. Previous studies also suggested that velocity reduction in this layer may vary from SW to NE, though by how much and in which direction is unclear. Avants et al. (2006) suggest a decrease from -3 to -6.5% moving northeastwards while Lay et al. (2006) instead suggest an *increase* in velocity from -4 to -0.6% in this direction. It should be noted that the reflected phases used in these studies, as we show here, have strong trade-offs between layer height and velocity variation, thus attempts to uniquely constrain height and velocity variation should be taken with caution.

This area has also been shown to contain additional structure above the basal ULVZ which has been interpreted as representing a fast lens of post-perovskite material within a slow velocity LLVP (Avants et al., 2006). This would explain the complex waveforms of alternating polarity indicative of fast and slow layers we observe in this region (Figure 6d and e).

5.1.3. Broader eastern region

Two studies consider broader-scale structure to the east of the Hawaiian islands, making use of the western section of the USArray as we do in this study. Sun et al. (2019) use (ScS-S)^{diff} arrival times and waveforms to model an 80km high, -15% velocity feature with a ramped triangular shape. This model is geographically consistent with the feature we observe in CBP stacked data just east of the Hawaiian islands (Figure 9a b). However trade-off curves indicate that a velocity reduction of 15% leads to a structure only 20 km high in this region (Figure 7d).

Zhao et al. (2017) develop and apply the ScS flip-reverse stacking method used here and model waveforms to map out structure in the eastern region of our study area. They find best-fitting structure of variable height (10-20km) with strong velocity reductions of 30%. While modeling of such structure is non-unique they do suggest that in some cases a gradational top to the ULVZ layer may be required, and in others a fast-velocity layer above the basal ULVZ is suggested. A gradational top would be consistent with our observations of small amplitude pre/post-cursors compared to those predicted for a 1D sharp-topped model, while the presence of an overlying fast velocity may explain the negative arrivals seen directly on top of mapped features in CBP stacks (Figure 6).

5.2. Height/Velocity trade-offs: Topography or variable velocity?

We have emphasised the trade-offs in our data when interpreting ULVZ parameters: the timings of the pre/post-cursors across the CBP stacks could be due to variable height, variable velocity contrast or a combination of the two.

If we assume that all ULVZ material has a constant velocity contrast of -20% Vs (within the range of previous estimates and the more likely models identified in HV stacks, Figure 7a), we can explain observations with variable topography ranging from 5 - 20 km in height (Figure 8a). While heights vary with assumed velocity reduction, within a realistic range of values heights are unlikely to be taller than ≈30 km, unless the ULVZ shows weak velocity reductions of less than 5% (which are unlikely to produce the pre/post-cursors observed here).

Alternatively, if we assume imaged structure is of constant height, we could explain variation of arrival times by variation in velocity contrasts within the ULVZ material. HV stacks show there is only a very limited range of heights which could explain all areas analysed based on identified trade-off curves (≈8-12km, Figure 7a - grey bar). Constraining the ULVZ layer to a constant height of 10 km, would require the material to be strongly heterogeneous with variations in velocity contrast from -5 to -48.5% (Figure 8b).

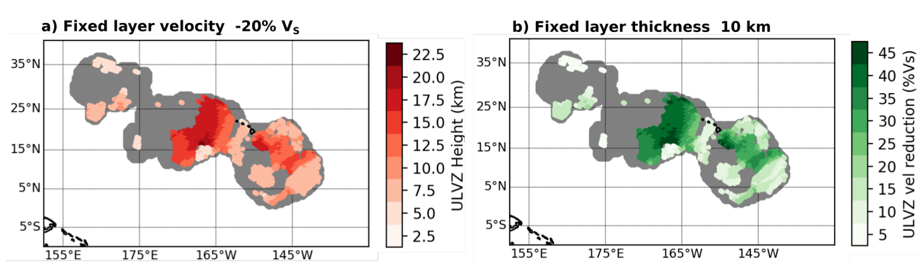

Figure 8: a) Predicted ULVZ heights based on pre/post-cursor arrivals imaged in CBP stacks assuming a layer of constant velocity contrast of -20%. b) Predicted ULVZ velocity contrasts assuming a layer of constant height of 10km.

Given the large range of velocity reductions required to explain the timing of arrivals we feel it is unlikely that observations reflect changes in velocity contrast alone. Geodynamic modeling of ULVZs, both as partial melt or as a chemically distinct dense material, predict variable topography of ULVZ thickness (Hernlund and Jellinek, 2010; Li et al., 2017), particularly in regions of strong regional convection such as plume upwellings like Hawaii. Additionally, any variations in ULVZ velocity would likely be linked to variation in ULVZ density, and therefore result in topographic changes. Given this, it is reasonable to interpret varying ULVZ layer thickness to be the main contributing factor to pre/post-cursors time variations observed across our study region, though in reality there is likely some combination of varying height and topography that fully explains observations.

5.3. A regional ULVZ layer of variable Topography: Geodynamic implications

ULVZ topography is likely to be controlled by a combination of factors: characteristics of ULVZ material (state, density and viscosity), wider mantle structure and flow (LLVPs, impinging slabs and upwelling plumes) and potentially CMB topography.

End member hypotheses assume that ULVZs represent either chemically distinct material or areas of partial melt. If ULVZs are due to partial melt, they would be predicted to form in the areas of highest CMB temperature within LLVP piles, and show relatively symmetric profiles in cross-section (Li et al., 2017). In contrast ULVZs of denser material, distinct from that of LLVPs, are predicted to accumulate at LLVP margins (e.g. McNamara et al., 2010) in discontinuous patches of variable shape and size (Li et al., 2017). The location of the Hawaiian ULVZ at the edge of the Pacific LLVP and the highly variable and non-symmetric shape we image is more in line with a distinct dense material rather than the presence of partial melt. ULVZ asymmetry is particularly clear in the reduction in height of the eastern ULVZ pile towards the LLVP interior

(Figure 6 section-2). A similar structure is predicted by 3D spherical models containing a distinct dense ULVZ material, and is explained by different magnitudes of viscous coupling between the hotter LLVP and cooler mantle side of the pile (Li et al., 2017).

Geodynamic modelling has shown increasing the density of ULVZ material leads to piles with greater lateral extent and smaller height (McNamara et al., 2010; Bower et al., 2011), while increasing the viscosity of material leads to taller piles in a convecting mantle (Hier-Majumder and Revenaugh, 2010). Thus the great lateral extent (1000s km) and small heights (10-20km) we observe in the western mega-ULVZ indicates a dense but not highly viscous ULVZ material.

Mega-ULVZs have been hypothesised to be the origin for high ^{3}He/^{4}He and low ^{182}W/^{184}W ratios observed in several hotspot locations including Hawaii (Mundl et al., 2017). Entrainment of material from the ULVZ might also explain variation of Pb isotope ratios observed in Hawaiian basalts (Harrison et al., 2017). However it is unclear if entrainment would occur if the ULVZ material is significantly dense (Bower et al., 2011). Jones et al. (2019) suggest that the presence of ultra-dense material could lead to the formation of larger plumes with increased thermal buoyancy, allowing the entrainment of small amounts of dense ULVZ material by viscous coupling with the hot upwelling mantle rather than via thermal buoyancy.

Surrounding mantle structure is likely to significantly affect ULVZ morphology. Geodynamic models have shown that compositionally distinct ULVZ material is likely to be thickest in piles formed beneath upwelling plumes rising from the edges of LLVPs (e.g. McNamara et al., 2010; Li et al., 2017). Based on our observations this suggests the plume conduit is off-set to the west of Hawaii, coincident with the thick western mega-ULVZ. This conclusion is supported by the recent global P-wave tomographic model of Hosseini et al. (2020) which has a high degree of sensitivity to CMB structure due to inclusion of core grazing P_{diff} phases. They observe a near-vertical plume centred slightly southwest of the surface hotspot, rising from a strong slow-velocity region on the CMB coincident with our imaged western mega-ULVZ.

Subducted material is also likely to play a significant role in ULVZ morphology. Where negatively buoyant subducted material interacts with LLVPs (and presumable also associated ULVZ structures at their margins), it is predicted to push material up into higher, steeper sided piles and potentially aid in plume generation (e.g. Heyn et al., 2020). We note that the highest parts of the regional Hawaiian ULVZ structure imaged here are bounded by the Pacific LLVP to the south and by small fast regions imaged in tomographic models to the north (Figure 9b). The study of Sun et al. (2019), modeled the high Eastern pile of ULVZ material as a ramped shape, and suggested slab debris is impinging and thickening ULVZ material here. Our observations suggest this may also be occurring at the NW edge of the mega-ULVZ.

Finally the height of a ULVZ layer is measured relative to the CMB, which may itself show significant topography. The recent study of Heyn et al. (2020) find that short wavelength topography is predicted at the edge of dense LLVP piles, caused by an interaction of the LLVP, plume upwellings and impinging slabs. How ULVZ material would interact with the LLVP along-margin depression they predict is currently unclear, but we might expect ULVZ material to pond within and potentially enhance existing depressions if it were significantly dense.

5.4. Small Amplitude pre/post-cursor arrivals

We observe several regions of clear ScS pre/post-cursors which all show arrival amplitudes significantly smaller than those predicted for the range of models within the trade-off curves defined by arrival times (Figure S7). Pre/post-cursor amplitudes are strongly affected by layer height, velocity contrast and event-station separation (see SM Section 1) which are accounted for in our synthetic models. However there are a range of additional factors which affect arrival amplitude and may contribute to the small amplitudes observed, including:

- CMB topographic depressions - causing enhanced ScS amplitudes (and thus smaller pre/post-cursor relative amplitudes) due to focusing effects (Wu et al., 2014)
- A diffuse ULVZ upper boundary - reducing pre/post-cursor boundary reflectively
- Variable internal ULVZ velocity structure - a weaker velocity contrast across the upper boundary affecting amplitudes while a stronger basal velocity reduction increases the delay time across the entire layer
- 3D ULVZ topography - leading to reduced coherency of pre/post-cursors in stacks
- Unknown ULVZ density - weak density contrasts reduce the impedance contrast and therefore reflection coefficient at the ULVZ boundary

These possibilities are explored in more detail in supplementary section S6. We find that reducing ULVZ density (from the +10% anomaly assumed in our synthetics), cannot explain the small amplitudes observed. A strongly diffuse upper ULVZ boundary (thickness 20-25km) could explain the amplitudes observed in the mega-ULVZ (stacks B and C Figure 8), but cannot reproduce weaker amplitudes observed to the east (stacks D,E and F). Recent work using high frequency S_{diff} observations has found evidence of increasing velocity reduction with depth within the Hawaiian ULVZ (Li et al., 2019), consistent with the diffuse boundary and variable internal structure options considered. Our observations indicate variable ULVZ topography, which likely contributes to observed amplitude reductions, especially since the Fresnel zones at data bounce-points (Figure S2) is broader than observed topography. We also find that ScS amplitudes are generally larger than predicted (Figure S8), which could indicate focusing due to CMB topography, likely contributing to small pre/post-cursor relative measurements.

Pulling apart the multiple factors that affect arrival amplitude is difficult, and it's likely that a number of the explanations posited contribute to the small pre/post-cursors observed.

6. Conclusion

Multiple previous studies have reported observations of 'the Hawaiian ULVZ'. Here we use broad-scale regional observations of ScS reflected waves and associated pre/post-cursors sensitive a wide area of the CMB near Hawaii to demonstrate the ULVZ is not a single distinct feature, but a regional-scale structure of varying topography. The large variation in previous ULVZ models may partially be explained by different studies imaging different parts of this variable large-scale feature.

We observe several distinct regions, Figure 9c:

- Western mega-ULVZ – roughly 2000 by 1000 km in size, likely 10-20km thick (but no taller than 30km).
- Eastern pile – an asymmetric pile of material 10-20km thick, increasing in thickness towards the NE away from the Pacific LLVP
- Complex southeastern region - containing a thin 5-10 km basal ULVZ layer, with complex waveforms indicative of alternating fast/slow layers,

consistent with previous suggestions of an overlying post-perovskite lens in this area (Avants et al., 2006).

Based on predictions from geodynamic modelling, the location of the ULVZ at the edge of the Pacific LLVP and its asymmetric shape are more indicative of a ULVZ comprised of compositionally distinct dense material, rather than partial melt. The highly variable topography observed seems to reflect an interplay between the Hawaiian plume upwelling, the Pacific LLVP and impinging slab material. The thick pile of the western mega-ULVZ likely represents the base of the Hawaiian plume stem, which is offset to the southwest of the surface hotspot expression. Both this area and the thick Eastern pile are sandwiched between the edge of the pacific LLVP and fast wavespeed anomalies, that we interpret as representing slab fragments. This suggests that slabs can act to push ULVZ material into taller piles against the edge of the LLVPs, as previously suggested by Sun et al. (2019).

7. Acknowledgments

The authors would like to thank Dr. Tim Jones and Dr. Doyoeng Kim for helpful discussion which informed paper content. This project has received funding from the European Research Council (ERC) under the European Union's Horizon 2020 research and innovation programme (grant agreement No. 804071 -ZoomDeep). All data is open access and is accessible through the IRIS database. Waveform processing was conducted using the python library obspy (Beyreuther et al., 2010).

References

Avants, M., Lay, T., Garnero, E.J., 2006. A new probe of ULVZ S-wave velocity structure: Array stacking of ScS waveforms. Geophysical research letters 33.

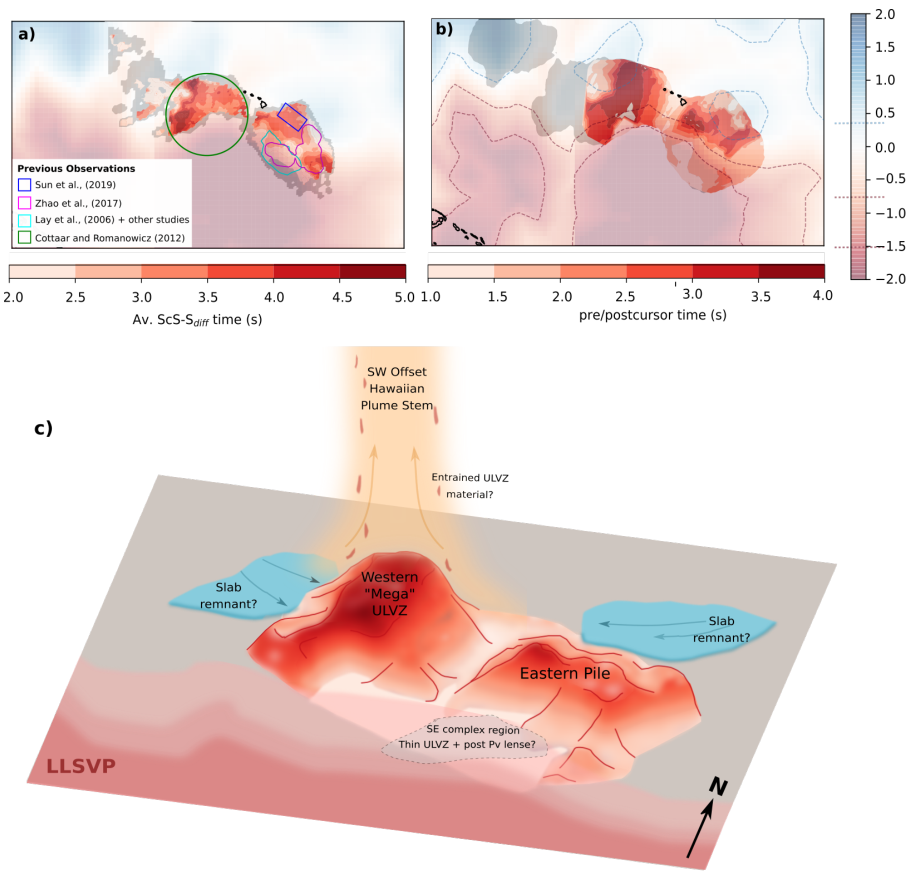

Figure 9: a) Coloured contours of geographical binned 3D corrected (ScS-S)^{diff} delay times averaged over 5 different tomographic model corrections. Grey regions show limits of data coverage. Coloured outlines highlight models of ULVZ structure from previous studies as labeled in the key. Background colours show tomographic model GyPSuM (Simmons et al., 2010) at the CMB. b) Coloured contours of pre/post-cursor arrival times imaged in CBP stacks. Dashed contours at -1.5% and -0.75% delineate the edge of the Pacific LLVP, while the +0.35% contour highlights regions of fast anomalies which may represent slab remnants. C) Summary Cartoon of interpreted large-scale ULVZ structure.

Beyreuther, M., Barsch, R., Krischer, L., Megies, T., Behr, Y., Wassermann, J., 2010. ObsPy: A python toolbox for seismology. Seismological Research Letters 81, 530–533.

Bower, D.J., Wicks, J.K., Gurnis, M., Jackson, J.M., 2011. A geodynamic and mineral physics model of a solid-state ultralow-velocity zone. Earth and Planetary Science Letters 303, 193–202.

Buffett, B.A., Garnero, E.J., Jeanloz, R., 2000. Sediments at the top of earth's core. Science 290, 1338–1342.

Cottaar, S., Li, Z., 2018. An ultra-low velocity zone beneath the Galapagos hotspot. AGUFM 2018, DI53A–0043.

Cottaar, S., Romanowicz, B., 2012. An unsually large ULVZ at the base of the mantle near Hawaii. Earth and Planetary Science Letters 355, 213–222.

Crotwell, H.P., Owens, T.J., Ritsema, J., 1999. The TauP toolkit: Flexible seismic travel-time and ray-path utilities. Seismological Research Letters 70, 154–160.

Dziewonski, A.M., Anderson, D.L., 1981. Preliminary reference Earth model. Physics of the earth and planetary interiors 25, 297–356.

French, S., Romanowicz, B., 2014. Whole-mantle radially anisotropic shear velocity structure from spectral-element waveform tomography. Geophysical Journal International 199, 1303–1327.

Grand, S.P., 2002. Mantle shear–wave tomography and the fate of subducted slabs. Philosophical Transactions of the Royal Society of London. Series A: Mathematical, Physical and Engineering Sciences 360, 2475–2491.

Harrison, L.N., Weis, D., Garcia, M.O., 2017. The link between Hawaiian mantle plume composition, magmatic flux, and deep mantle geodynamics. Earth and Planetary Science Letters 463, 298–309.

Hernlund, J.W., Jellinek, A.M., 2010. Dynamics and structure of a stirred partially molten ultralow-velocity zone. Earth and Planetary Science Letters 296, 1–8.

Heyn, B.H., Conrad, C.P., Trønnes, R.G., 2020. Core-mantle boundary topography and its relation to the viscosity structure of the lowermost mantle. Earth and Planetary Science Letters 543, 116358.

Hier-Majumder, S., Revenaugh, J., 2010. Relationship between the viscosity and topography of the ultralow-velocity zone near the core–mantle boundary. Earth and Planetary Science Letters 299, 382–386.

Hosseini, K., Sigloch, K., Tsekhmistrenko, M., Zaheri, A., Nissen-Meyer, T., Igel, H., 2020. Global mantle structure from multifrequency tomography using P, PP and P-diffracted waves. Geophysical Journal International 220, 96–141.

Houser, C., Masters, G., Shearer, P., Laske, G., 2008. Shear and compressional velocity models of the mantle from cluster analysis of long-period waveforms. Geophysical Journal International 174, 195–212.

Hutko, A.R., Lay, T., Revenaugh, J., 2009. Localized double-array stacking analysis of PcP: D" and ULVZ structure beneath the Cocos plate, Mexico, central Pacific, and north Pacific. Physics of the Earth and Planetary Interiors 173, 60–74.

IRIS-DMC, 2015. Data services products: Synthetics engine. URL: `https://doi.org/10.17611/DP/SYNGINE.1`.

Jones, T., Davies, D.R., Sossi, P., 2019. Tungsten isotopes in mantle plumes: Heads it's positive, tails it's negative. Earth and Planetary Science Letters 506, 255–267.

Kim, D., Lekić, V., Ménard, B., Baron, D., Taghizadeh-Popp, M., 2020. Sequencing seismograms: A panoptic view of scattering in the core-mantle boundary region. Science 368, 1223–1228.

Kohler, M., Vidale, J., Davis, P., 1997. Complex scattering within D" observed on the very dense Los Angeles region seismic experiment passive array. Geophysical research letters 24, 1855–1858.

Labrosse, S., Hernlund, J., Coltice, N., 2007. A crystallizing dense magma ocean at the base of the Earth's mantle. Nature 450, 866–869.

Lay, T., Hernlund, J., Garnero, E.J., Thorne, M.S., 2006. A post-perovskite lens and D"heat flux beneath the central pacific. science 314, 1272–1276.

Lekic, V., Cottaar, S., Dziewonski, A., Romanowicz, B., 2012. Cluster analysis of global lower mantle tomography: A new class of structure and implications for chemical heterogeneity. Earth and Planetary Science Letters 357, 68–77.

Li, M., McNamara, A.K., Garnero, E.J., Yu, S., 2017. Compositionally-distinct ultra-low velocity zones on Earth's core-mantle boundary. Nature communications 8, 1–9.

Li, Z., Cottaar, S., Leng, K., 2019. High-frequency shear wave diffraction at Hawaii ULVZ. AGUFM 2019, DI41C–0011.

Ligorria, J.P., Ammon, C.J., 1999. Iterative deconvolution and receiver-function estimation. Bulletin of the seismological Society of America 89, 1395–1400.

Liu, J., Li, J., Hrubiak, R., Smith, J.S., 2016. Origins of ultralow velocity zones through slab-derived metallic melt. Proceedings of the National Academy of Sciences 113, 5547–5551.

Luo, S.N., Ni, S., Helmberger, D.V., 2001. Evidence for a sharp lateral variation of velocity at the core–mantle boundary from multipathed PKPab. Earth and Planetary Science Letters 189, 155–164.

McNamara, A.K., Garnero, E.J., Rost, S., 2010. Tracking deep mantle reservoirs with ultra-low velocity zones. Earth and Planetary Science Letters 299, 1–9.

Mori, J., Helmberger, D.V., 1995. Localized boundary layer below the mid-pacific velocity anomaly identified from a PcP precursor. Journal of Geophysical Research: Solid Earth 100, 20359–20365.

Mundl, A., Touboul, M., Jackson, M.G., Day, J.M., Kurz, M.D., Lekic, V., Helz, R.T., Walker, R.J., 2017. Tungsten-182 heterogeneity in modern ocean island basalts. Science 356, 66–69.

Nissen-Meyer, T., Driel, M.v., Stähler, S., Hosseini, K., Hempel, S., Auer, L., Colombi, A., Fournier, A., 2014. AxiSEM: broadband 3-d seismic wavefields in axisymmetric media. Solid Earth , 425–445.

Otsuka, K., Karato, S.i., 2012. Deep penetration of molten iron into the mantle caused by a morphological instability. Nature 492, 243–246.

Pradhan, G.K., Fiquet, G., Siebert, J., Auzende, A.L., Morard, G., Antonangeli, D., Garbarino, G., 2015. Melting of MORB at core–mantle boundary. Earth and Planetary Science Letters 431, 247–255.

Revenaugh, J., Meyer, R., 1997. Seismic evidence of partial melt within a possibly ubiquitous low-velocity layer at the base of the mantle. Science 277, 670–673.

Simmons, N.A., Forte, A.M., Boschi, L., Grand, S.P., 2010. GyPSuM: A joint tomographic model of mantle density and seismic wave speeds. Journal of Geophysical Research: Solid Earth 115.

Sun, D., Helmberger, D., Lai, V., Gurnis, M., Jackson, J., Yang, H.Y., 2019. Slab control on the northeastern edge of the mid-pacific LLSVP near Hawaii. Geophysical Research Letters 46, 3142–3152.

Tesoniero, A., Auer, L., Boschi, L., Cammarano, F., 2015. Hydration of marginal basins and compositional variations within the continental lithospheric mantle inferred from a new global model of shear and compressional velocity. Journal of Geophysical Research: Solid Earth 120, 7789–7813.

Thorne, M.S., Garnero, E.J., Jahnke, G., Igel, H., McNamara, A.K., 2013. Mega ultra low velocity zone and mantle flow. Earth and Planetary Science Letters 364, 59–67.

To, A., Fukao, Y., Tsuboi, S., 2011. Evidence for a thick and localized ultra low shear velocity zone at the base of the mantle beneath the central Pacific. Physics of the Earth and Planetary Interiors 184, 119–133.

Wu, W., Ni, S., Shen, Z., 2014. Constraining the short scale core–mantle boundary topography beneath Kenai Peninsula (Alaska) with amplitudes of core-reflected PcP wave. Physics of the Earth and Planetary Interiors 236, 60–68.

Yu, S., Garnero, E.J., 2018. Ultralow velocity zone locations: A global assessment. Geochemistry, Geophysics, Geosystems 19, 396–414.

Yuan, K., Romanowicz, B., 2017. Seismic evidence for partial melting at the root of major hot spot plumes. Science 357, 393–397.

Zhao, C., Garnero, E.J., Li, M., McNamara, A., Yu, S., 2017. Intermittent and lateral varying ULVZ structure at the northeastern margin of the pacific llsvp. Journal of Geophysical Research: Solid Earth 122, 1198–1220.

Zhu, L., Kanamori, H., 2000. Moho depth variation in southern california from teleseismic receiver functions. Journal of Geophysical Research: Solid Earth 105, 2969–2980.